

# Evaluation of Additive Friction Stir Deposition of AISI 316L For Repairing Surface Material Loss in AISI 4340

Louis Peter Martin (✉ [LPMGIS@RIT.EDU](mailto:LPMGIS@RIT.EDU))

Rochester Institute of Technology <https://orcid.org/0000-0002-1087-4698>

Allen Luccitti

Rochester Institute of Technology

Mark Walluk

Rochester Institute of Technology

---

## Research Article

**Keywords:** Additive Friction Stir Deposition, AFSD, AISI 316, Repair

**Posted Date:** January 6th, 2022

**DOI:** <https://doi.org/10.21203/rs.3.rs-1214920/v1>

**License:**   This work is licensed under a Creative Commons Attribution 4.0 International License.

[Read Full License](#)

---

# Abstract

Additive technologies provide a means for repair of various failure modes associated with material degradation occurring during use in aggressive environments. Possible repair strategies for AISI 4340 steel using AISI 316L deposited by additive friction stir deposition (AFSD) were evaluated under this research by metallography, microhardness, and wear and mechanical testing. Two repair geometries were investigated: groove-filling and surface cladding. The former represents repair of localized grinding to eliminate cracks, while the latter represents material replacement over a larger area, for example to repair general corrosion or wear. The 316L deposited by AFSD exhibited a refined microstructure with decreased grain size and plastic strain, lower strength, and lower hardness than the as-received feedstock. Wear testing by both two-body abrasion and erosion by particle impingement indicated that the wear resistance of the 316L cladding was as good as, or better than, the substrate 4340 material; however, there was some evidence that the resistance to intergranular corrosion was compromised due to the formation of carbides or sigma phase. In both repair geometries, the microstructure of the substrate beneath the deposited material exhibited heat affected zones that appeared to have austenized during the deposition process, and transformed to martensite or bainite during cooling. This report constitutes an initial evaluation of a novel approach to the repair of structural steel components damaged by microcracking, wear or corrosion.

## 1.0 Introduction

Additive friction stir deposition (AFSD) is a newly-developed additive materials technology that is receiving increasing interest for manufacturing applications in a variety of material systems [1, 2, 3, 4, 5, 6, 7, 8, 9, 10, 11, 12, 13, 14]. In AFSD, a feedstock material is fed through a rotating tool and axially loaded against a substrate. The load applied to the feedstock during feeding, combined with shear forces from the tool rotation, lead to frictional heating that softens the feedstock and substrate. The feed material extrudes into the space between the rotating tool and the substrate, and concurrent deformation and solid-state mixing occur in a surface layer within the substrate. As a result, a metallurgical bond is formed, without melting, between the filler and substrate alloys [1]. Translation of the tool along the surface generates a layer of deposited alloy, schematically illustrated in Fig. 1a, and subsequent additional passes can be performed to build up material through the deposition of additional layers. The method is mechanistically similar to the well-known joining technology, friction stir welding (FSW), and to a related additive technology, additive friction surfacing (AFS).

FSW uses a rotating, non-consumable tool with a profiled 'pin' that is plunged into the joint between two workpieces until a larger-diameter 'shoulder' reaches the surface. Heat generated by friction between the tool and the workpieces plasticizes the material around the pin. As the tool traverses along the joint line, the plasticized material is transferred from the leading edge to the trailing edge, thus forming a weld by solid state mixing. The high strains and comparatively low temperatures (typically  $0.6 - 0.9T_{\text{melt}}$ ) associated with the process result in microstructural refinement and improved mechanical properties in

the weld [-]. However, because FSW does not add material, but simply translates the plasticized material, it provides limited applicability to volumetric repairs.

Since the late 1990's, several technologies related to FSW have been developed to duplicate the beneficial microstructural effects of FSW in additive material applications [1]. In AFS, a consumable, rotating rod (mechtrode) of feed material is axially loaded against the surface of the substrate. Frictional heating and shear forces plasticize the rotating mechtrode, allowing for deposition of a layer of material as it is translated along the surface [1,21]. The material at the outer edge of the mechtrode is unconstrained, which allows radial and vertical extrusion of unbonded material, and material waste in the form of the resultant flash. In contrast, the AFSD tool constrains the feed material and transfers shear forces that drive the material flow, reducing waste and providing improved control of the deposition process.

Known commercially as MELD, AFSD has the potential to enable high-deposition rates during the manufacture of moderately complex geometries [3,4]. The resultant components exhibit fine equiaxed microstructures that provide enhanced wear resistance, corrosion protection, and mechanical properties [5,21, 22]. The first reported applications of AFSD were for additive manufacturing of aluminum and magnesium alloys [6,7], and additional results were later reported for Inconel 625 [8,9], alloy Ti-6Al-4V [11], copper [10], and aluminum-matrix composites [4]; however, published results for steels are limited [11,-25]. Because the solid-state material transfer promotes strong metallurgical bonding while mitigating hot cracking, porosity, heat affected zone (HAZ), and high residual stresses that can be associated with fusion processes, AFSD has obvious potential for repair applications. However, this aspect of the technology is also largely absent from the published literature [13,-].

The present study will evaluate possible repair strategies for AISI 4340 steel using AISI 316L deposited by AFSD. Two repair geometries were investigated: surface cladding (Fig. 1a) and groove-filling (Fig. 1b). The latter represents repair of localized grinding to eliminate cracks, while the former represents material replacement over a larger area, for example to repair general corrosion or wear. The substrate material, AISI 4340, is a medium-carbon, low alloy steel of interest for its broad use in applications requiring high strength and toughness, while the AISI 316L filler is an austenitic stainless steel that was selected based upon corrosion resistance and prior experience with deposition via AFSD.

## **2.0 Materials And Experimental**

### **2.1 Materials**

The AFSD feed material was a solid square rod of AISI 316L, with dimensions of 9.4 mm x 9.4 mm and an average measured hardness of 24 HRC (257 HV0.2). The square profile of the feedstock facilitates transfer of torque from the tool to the feedstock, allowing the tool to drive rotation of the feedstock. Prior to deposition, the feedstock was lubricated with graphite to reduce friction with the tool. The substrate material was AISI 4340 plate with a nominal thickness of 11.5 mm and a specified minimum hardness of 42 HRC (425 HV0.2). Four grooves were machined into the surface of the plate with the dimensions

indicated in Table 1. The nominal compositions of the feedstock and substrate alloys are provided in Table 2.

**Table 1:** Dimensions of the grooves in the plate.

Groove ID	Met. Sample	Depth, mm	Width, mm	Radius, mm
1	G1	0.76	4.11	3.18
2	G2	1.52	5.44	3.18
3	G3	0.76	6.02	6.35
4	G4	1.52	8.26	6.35

**Table 2:** Specified composition of the steel substrate and feedstock alloys.

Alloy	C	Mn	P	S	Si	Ni	Cr	Mo	Source
AISI 4340	0.38– 0.43	0.60– 0.80	0.035	0.040	0.15– 0.35	1.65– 2.00	0.70– 0.90	0.20– 0.30	ASTM A322-13
AISI 316L	0.03	2.00	0.045	0.030	0.75	10.0– 14.0	16.0– 18.0	2.00– 3.00	ASTM A666-15

\* All values are maxima unless otherwise indicated.

## 2.2 Additive Friction Stir deposition (AFSD)

AFSD was performed by MELD Manufacturing Corporation (Christiansburg, VA, USA) on a MELD B8 system with a 39 mm diameter tool head. Three different deposition geometries were executed: single-width cladding, overlap cladding, and groove-filling. The cladding and groove-filling configurations are illustrated schematically in Fig. 1, where the tool translation direction in Fig. 1b is normal to the plane of the image. Note from Fig. 1a that, as the rotating tool is translated, on one side of the tool the rotation is in the translation direction, and on the other side it is away from it. These two sides are described as ‘advancing’ and ‘retreating’, respectively.

Table 3 shows the process parameters used in the initial passes for each geometry. The parameters were designed to fill the groove on the 1st pass by scaling the tool translation speed  $V_{tool}$  and feedstock feed rate  $V_{feed}$  to provide a deposition rate  $R_{dep}$  (mm<sup>3</sup>/s) equal to approximately 1.6x – 2.8x the volume of the groove and substrate-tool gap transited by the tool each second,  $R_{groove} + R_{layer}$  (also mm<sup>3</sup>/s), where the excess material was applied to ensure complete filling of the grooves and to increase the pressure below the tool in order to maximize shearing of the substrate. The process parameters are interrelated via the relationships:

$$R_{dep} \left[ \frac{mm^3}{s} \right] = A_{feed} [mm^2] \cdot V_{feed} \left[ \frac{mm}{s} \right]$$

1

$$R_{groove} \left[ \frac{mm^3}{s} \right] = A_{groove} [mm^2] \cdot V_{tool} \left[ \frac{mm}{s} \right]$$

2

$$R_{layer} \left[ \frac{mm^3}{s} \right] = W_{dep} [mm] \cdot z_{step} [mm] \cdot V_{tool} \left[ \frac{mm}{s} \right]$$

3

**Table 3:** AFSD parameters for the groove fill-passes, and for the cladding application.

Groove Number	1	2	3	4	Cladding
Groove Cross-Section, $A_{groove}$ , mm <sup>2</sup>	2.1	5.9	3.1	8.6	N/A
Tool Rotation Rate, $w$ , RPM	500				
Feedstock Feed Rate, $V_{feed}$ , mm/s	0.5				
Tool Translation Speed, $V_{tool}$ , mm/s	1.7	1.7	1.8	1.8	3.4
Layer Thickness, $z_{step}$ [mm]	0.5				
Layer Cross-Section, $W_{dep} \cdot z_{step}$ , mm <sup>2</sup>	7.3				
Deposition Rate, $R_{dep}$ , mm <sup>3</sup> /s	44.4				
Volume of groove at Traverse Rate, $R_{groove}$ , mm <sup>3</sup> /s	3.6	9.9	5.5	15.3	N/A
Volume of Layer at Traverse Rate, $R_{layer}$ , mm <sup>3</sup> /s	12.3	12.3	12.9	12.9	24.7
Fill Volume Rate, $R_{groove} + R_{layer}$ , mm <sup>3</sup> /s	15.9	22.2	18.4	28.2	24.7
Fill Ratio, $R_{dep} / (R_{groove} + R_{layer})$	2.8	2.0	2.4	1.6	1.8

where  $A_{feed}$  and  $A_{groove}$  are the cross-sectional areas of the feedstock and the groove, respectively,  $W_{dep}$  is the width of the deposited material, and  $z_{step}$  is the nominal layer thickness as determined by the increment in the z-coordinate of the tool between passes. Note that for the 1st, filling pass, the base of the

tool was set to a height approximately 0.5 mm above the surface of the substrate. In subsequent passes,  $V_{\text{feed}}$  and  $V_{\text{tool}}$  were manually adjusted to maintain the ratio of  $R_{\text{dep}}$  to  $R_{\text{groove}} + R_{\text{layer}}$  between 1.8 and 2.9.

The photograph in Fig. 2a shows the four filled grooves (#1 – #4) at the top, and a single-width multipass cladding (SC) at the bottom. Fig. 2b shows a region of overlap cladding at the bottom. Both images show the locations from which samples were removed for metallographic cross-sections (G1 – G4, and O1 – O4), tensile testing (T1 – T6), bend testing (S1), or wear testing (W1 – W4).

## 2.3 Metallurgical Inspection

Samples were removed from the plate by electrical discharge machining, polished to 1  $\mu\text{m}$  diamond suspension, and etched to reveal the microstructure. The AISI 4340 alloy was etched with nital or Vilella's reagent, while the AISI 316L was chemically etched with Kalling's reagent or electrolytically etched in 10% oxalic acid. Vickers microhardness testing was performed on a LECO AMH55 with a 200 g load and 13 s hold time.

### 2.4 Mechanical Testing

Tensile and 3-point bend testing were performed using a 100 kN load cell on an Instron 8801 servo-hydraulic testing system. Tensile specimens used a gauge length of approximately 12.5 mm, with the rest of the dimensions derived from the guidelines provided by ASTM B557 for rectangular sub-sized specimens [30]. The samples were oriented transverse to the filled grooves, and were cut from the plate by electrical discharge machining. The sample thickness was approximately 0.76 mm for samples T1 – T3, and 1.52 mm for samples T4 – T6. In addition, a set of tensile samples was machined from an additional single-width multipass cladding (not shown in Fig. 2). Those samples were axially oriented parallel to the AFSD direction, and were comprised solely of the AFSD 316L material. All tensile testing was performed at an extension rate of 0.085 mm/s. Bend testing was performed on the section labelled S1 in Fig. 2b with an 85 mm span and a load rate of 74.1 N/s.

### 2.5 Wear Testing

Two-body wear testing was performed in compliance with the ASTM G174 loop abrasion test (Bud Labs, Rochester, New York 14616) [31]. The testing used a 100g load and a 30 mm alumina abrasive tape for a duration of 75 belt passes. Four tests were performed at each location indicated W1 – W3 in Fig. 2. For comparison, erosion testing was performed (Bud Labs, Rochester, New York 14616) in compliance with the ASTM G76 test for erosion by solid particle ( $\text{Al}_2\text{O}_3$ ) impingement using gas jets using the following test parameters: standoff 10 mm, impingement angle  $10^\circ$ , gas pressure 55.2 kPa, and gas flow rate 118  $\text{cm}^3/\text{s}$  [32]. Three tests were performed at each of two locations, W1 and W4, in Fig. 2.

## 3.0 Results And Discussion

### 3.1 Characterization of Substrate and Feedstock

Light optical microscopy (LOM) images of the as-received microstructure in the AISI 316L feedstock are shown in Figs. 3a and 3b. The microstructure consists of coarse austenitic grains, typically 50 – 100  $\mu\text{m}$ , that contain twins and shear bands associated with prior cold work equivalent to approximately 10% reduction [33]. LOM and scanning electron microscope (SEM) images of the as-received microstructure in the AISI 4340 substrate are provided in Figs. 3c and 3d, respectively. The observed microstructure consists of tempered martensite, and is consistent with the nominal hardness of 42 HRC.

Table 4 provides the measured yield strength, tensile strength, and hardness in the substrate and filler feedstock, along with specified values related to tempering of the 4340 or cold work in the 316L. The measured hardness of 426 HV0.2 in the 4340 substrate, which corresponds to 43 HRC per ASTM E140-02 [34], is again consistent with the specified minimum of 42 HRC. The measured hardness is also consistent with the measured yield and tensile strengths of 1286 and 1368 MPa, respectively, and corresponds to a tempering temperature of approximately 500 °C for two hours [35]. In the 316L feedstock, the measured tensile strength of 724 MPa approximately correspond to a 1/8-hard condition per ASTM A666-15 [36].

**Table 4:** Results of tensile and hardness testing of the as-received substrate and feedstock alloys, along with published values for different temper/cold-work conditions.

Material	Condition	Yield Strength, MPa	Tensile Strength, MPa	HRB/C	HV	Source
4340	Substrate	1286	1368	43C, avg.	426	Measured
	Temper 205 °C	1860	1980	53C, max.	560	Ref. 30
	Temper 315 °C	1620	1760	50C, max.	513	
	Temper 425 °C	1365	1500	46C, max.	458	
	Temper 540 °C	1160	1240	39C, max.	382	
	Temper 650 °C	860	1020	31C, max.	310	
	Temper 705 °C	740	860	24C, max.	260	
316L	Feedstock	586	724	24C, avg.	257	Measured
	Annealed	205	515	95B	-	Ref. 31
	1/8 hard	380	690	-	-	
	1/4 hard	515	860	-	-	
	1/2 hard	760	1035	-	-	

## 3.2 AFSD Groove-Filling

Fig. 4 shows LOM images of metallurgical cross-sections from the AFSD groove-filled locations G1 – G4, indicated in Fig. 2a. The sections have been etched with nital, which reveals the microstructure in the 4340 substrate but has no effect on the 316L filler. The images show the deformation of the groove geometry to be asymmetrical, with more deformation on the advancing side of the tool (corresponding to the left side of the images). This is consistent with prior reports of asymmetry in the interfacial mixing during deposition of AA2024 on AA6061, where the asymmetry was attributed to the interaction between the in-plane material expansion (driven by compression of the feedstock) and the material flow (driven by rotation of the tool head) [12]. In addition, the deformation is more pronounced in the smaller-radius grooves 1 and 2 (Figs. 4a and 4b) than in larger-radius grooves 3 and 4 (Figs. 4c and 4d). This suggests that the lateral constraint formed by the smaller radius transfers the shear forces to the substrate more effectively. Both of the deeper grooves, Figs. 4b and 4d, experienced cracking or lack of fusion at the interfaces, indicated by the white arrows in Fig. 4. This is shown in more detail in Fig. 5, where the images reveal different behavior in the two groove geometries. The smaller diameter groove 2 in Fig. 5a exhibits lack of fusion in the deeper parts of the groove (lower right) and well-bonded interface with localized cracking of the substrate in the shallower parts (upper left). In contrast, the larger diameter groove 4 in Fig. 5b exhibits lack of fusion along most of the substrate-filler interface. The feature indicated by the dark arrow in Fig. 5a is a trail of carbide inclusions the AFSD 316L introduced during the stir process.

Beneath the filled grooves, the microstructure shows two distinct layers of HAZ that vary in depth and relative thickness for the different geometries. The microstructures shown in Fig. 6 correspond to the four numbered locations in Fig. 4a: 1) 316L AFSD filler, 2) HAZ1, 3) HAZ2, and 4) substrate. Compared to the as-received 316L microstructure (Figs. 3a and 3b), the microstructure in the AFSD 316L (Fig. 6a) is significantly refined, with grain size  $<25\ \mu\text{m}$  and minimal twinning. The HAZ1 microstructure in Fig. 6b is predominantly martensitic, indicating that the region austenized above  $\sim 727\ ^\circ\text{C}$ , then transformed to martensite during rapid cooling [1]. The presence of martensite suggests decreased toughness near the interface. At the bottom of HAZ1 there is a gradual transition to the HAZ2 microstructure (Fig. 6c), which is comprised of coarse carbides consistent with upper bainite. This suggests that the HAZ2 region austenized, but did not cool rapidly enough to form martensite. In addition, HAZ2 has a significant gradient in the grain size or coarseness of the structure, with the bottom of HAZ2 being finer than the initial tempered martensitic structure found in the substrate. This further supports the idea that HAZ2 austenized during the process, with higher maximum temperatures resulting in larger grains closer to the surface. Finally, the microstructure in the substrate below HAZ2 (Fig. 6d) is consistent with the as-received microstructure in Figs. 3c and 3d. SEM images of the microstructures at the bottom of HAZ2 and the top of the underlying substrate are shown at higher magnification in Figs. 7a and 7b, respectively. The images confirm the bainitic structure in the HAZ2 to have a finer overall morphology than the substrate, implying a low austenizing temperature, with islands of hypoeutectoidal ferrite.

Fig. 8 shows the results of microhardness depth profiling at the locations indicated by the dashed lines in Figs. 4a and 4b. The data show the hardness of the AFSD 316L to be approximately 88% of the original

feedstock, 225 HV0.2 versus 257 HV0.2 from Table 4. This decrease in hardness is associated with dynamic recrystallization that occurs during the AFSD process, leading to the competing effects of relaxation of the strain hardening and decrease in grain size. In HAZ1 the hardness is substantially elevated, exceeding 600 HV0.2 and approaching the maximum quenched hardness of ~670 HV for 0.38% carbon steel [1]. This hardness is consistent with the largely martensitic microstructure observed in Fig. 6b. The HAZ2 hardness ranges from ~347 HV0.2 near the boundary with HAZ1 to ~405 HV0.2 at the boundary with the substrate microstructure, with the gradient being attributed to the observed trend in grain size discussed above. Finally, the hardness in the substrate below HAZ2 ranges from ~340 HV0.2 near HAZ2 to the baseline value of ~426 HV0.2 reported in Table 4. This gradient near the boundary with HAZ1 does not correlate with any visible microstructural changes, and is attributed to partial stress relieving and tempering that occurs at temperatures between 595 °C and 675 °C [37]. The hardness data are consistent across the different locations in the two samples, and are summarized in Table 5.

**Table 5:** Vickers microhardness results from the depth profiles in Fig. 8, but segregated by test location. ‘n’ refers to the number of measurements.

		Grooves (Fig. 8)			Overlap Clad (Fig. 13)		
		n	Average	St. Dev.	n	Average	St. Dev.
316	AFSD	41	225	30	16	249	47
4340	HAZ1	9	637	30	20	605	49
4340	HAZ2	38	386	29	16	392	17
4340	Substrate	92	424	16	98	417	11

The observed HAZ’s are the result of a complex thermal profile resulting from the rapid heating, short term exposure at the maximum temperature, and air cooling during each of the multiple AFSD passes. The two zones are differentiated by the maximum temperature attained, which was higher near the surface, and by the cooling rate, which was faster near the surface. These factors interact to affect the extent of austenization, the prior austenitic grain size, and the formation of bainite versus martensite. The presence of martensite in HAZ1 suggests that the material transformed to austenite, then cooled sufficiently rapidly to inhibit the formation of bainite. Similarly, the gradient in the grain size in HAZ2, as well as the refined grain size relative to the original microstructure, suggest that the alloy reached a lower transformation temperature, and cooled less rapidly than HAZ1, with the net effect of converting the original tempered martensite primarily to upper bainite.

The difference in hardness between the AISI 4340 substrate and the AFSD filler metal creates certain implications with respect to mixing at the interface. For example, comparison of the deposition patterns in Fig. 4 with prior published work relating to more evenly matched, and softer, alloys suggests unusually distinct interfaces in the current samples [12,13]. In fact, prior work on AFSD and FSW has defined several characteristic microstructural zones associated with solid state friction processes: stir zone (SZ),

thermomechanical affected zone (TMAZ), heat affected zone (HAZ), and base metal (BM) [14,16]. The TMAZ refers to regions where the substrate material has been plastically deformed, with evidence of material flow, breakup of inclusions, and distortion of interfaces or boundaries. This region is generally absent from the observed microstructures for 316L AFSD on AISI 4340. This is illustrated in Fig. 4, where the visible deformation of the substrate is limited to localized distortion of the grooves, mostly on the advancing side of the first pass (the left side of the images). As a result of the apparent lack of shear deformation, the extent of mixing of the substrate and filler alloys at the interface was evaluated further.

Fig. 9 shows LOM images from the left edge of groove 1 in section G1, and from the right edge of groove 3 in section G3. As with the prior images, the reagent that was used to etch the substrate has no effect on the 316L filler alloy, thus providing a strong contrast between the two materials. The resultant images show evidence of localized mixing, with visible trails of substrate alloy entrained into the filler metal. The observed mixing is typically short-range at the interface, <50 mm, with some evidence of longer-range entrainment of substrate alloy into the AFSD 316L visible in the upper-half of Fig. 9b. To further reveal this aspect of the mixing, the AFSD 316L filler was electrolytically etched in oxalic acid for 90 s at 1.0 A/cm<sup>2</sup>. This etching condition is designed to reveal possible sensitization due to depletion of Cr from the grain boundaries [39]. The resultant microstructures are shown in Fig. 10 for the area from Fig. 9a. The thickening of the grain boundaries in the filler alloy indicated by '1' in Fig. 10b suggests the early stages of potential sensitization, which can be associated with the formation of carbides due to the ingress of C from the graphite lubricant, or to the formation of sigma phase that has been reported to occur during friction stir processing of AISI 316L [40]. The effect is generally localized to the interfaces between the substrate and filler, indicated by '1' in Fig. 10b and highlighted in Fig. 10c, and between subsequent AFSD passes, indicated by '2' in Fig. 10a. Away from these regions, for example at '3' in Fig. 10b, the etching does not significantly attack the filler alloy, except for a few areas with the appearance of shear-driven flow, location '4' in Fig. 10a. Note that while the localized thickening of the grain boundaries does indicate some degree of decreased resistance to corrosion relative to the unaffected parts of the filler, the oxalic acid etch is a sensitive screening test that may detect conditions which are not necessarily detrimental from a performance perspective [39]. As such, further investigation is required to develop a fuller understanding of the corrosion performance of AFSD 316L, and the potential role of lubricants used during the process.

Tensile testing was performed on sub-sized specimens extracted from grooves 1 and 3, and oriented perpendicular to the AFSD/groove axis. The thickness of the specimens from groove 1, T1 – T3, was targeted to match the depth of the groove in order to isolate the contribution of the AFSD filler and the filler-substrate interfaces. In contrast, the thickness of the specimens from groove 3, T4 – T6, targeted approximately equal amounts of filler and substrate. The results tabulated in Table 6 show the average yield and tensile strengths for the groove 1 specimens to be 516 and 725 MPa, respectively, while those from groove 3 are 645 and 1391 MPa, respectively.

**Table 6:** Results of tensile testing AFSD locations perpendicular grooves 1 and 3, with additional data parallel to a thick multi-pass cladding.

Location	Orientation	Sample ID**	Yield Strength, MPa	Tensile Strength, MPa
Groove 1	Transverse	T1	513.7*	717.3
		T2	489.5	709.6
		T3	542.6	747.4
Groove 3	Transverse	T4	674.3	1345.1
		T5	621.2	1404.9
		T6	640.5	1424.3
Cladding 316L only <sup>+</sup>	Axial	N/A	591.6	634.2
		N/A	405.4	695.2
		N/A	561.3	618.4

\* Estimated from cross-head displacement due to malfunction of extensometer.

\*\* From Fig. 2

<sup>+</sup> Not shown

Fig. 11 shows the fracture cross-sections for samples T1 from groove 1 and T5 from groove 3. The images show ductile necking in the AFSD filler (top), with minimal deformation in the harder substrate (bottom). The T1 sample is shown in Fig. 11a, to be predominantly filler alloy (~80%), while the T5 sample is approximately one-half substrate (~50%), which accounts for the elevated strength values. Assuming a linear rule of mixtures, a simple linear regression can be used to estimate the tensile strength of the 4340 substrate and 316L filler as 1599 and 524 MPa, respectively. For the 316L filler, this corresponds to a well-annealed condition per Table 4, which is not surprising given the microstructure observed in Fig. 6. For the 4340 substrate, the interpretation is more challenging due to the non-uniform microstructure discussed above. However, the data indicate that immediately below the grooves, the substrate material has an elevated tensile strength, which is consistent with the elevated hardness and the observed martensitic microstructure. In both samples, the fracture propagated through the filler alloy, rather than along the interface with the substrate, and occurred at approximately the minimum thickness of the underlying substrate material. This indicates that, for this test geometry, the interfaces are at least as strong as the filler alloy. For comparison, an additional set of tensile tests was performed on samples extracted from a thick single-width cladding, and oriented axially along the AFSD deposition direction. Those samples, which were comprised solely of AFSD alloy with no attached substrate material, had average yield and tensile strengths of 519 and 649 MPa, respectively.

### 3.3 AFSD Cladding

Surface cladding by AFSD was also explored as a potential method suitable for material replacement over larger areas. Fig. 2b showed a region of cladding that was deposited with approximately 20% overlap between passes. Four metallurgical samples prepared from the locations identified as O1 - O4 in Fig. 2b are shown in Fig. 12. The cross-sections show a similar HAZ pattern comprising two layers with microstructures comparable to those previously shown in Fig. 6. Hardness depth profiles performed at the locations indicated by the dashed lines in Figs. 12c and 12d are presented in Fig. 13. The depth profiles are comparable to those from the groove-filling geometry presented in Fig. 8, with a slight decrease in the hardness of the filler material relative to the as-received condition, HAZ1 hardness again in excess of 600 HV0.2, HAZ2 hardness averaging 392 HV0.2, and BM hardness increasing from a minimum near HAZ2 to the baseline measured in the as-received plate. In general, HAZ1 is thicker than in the groove-filling examples from Fig. 8, while HAZ2 is less pronounced and lacks the measureable gradient between the boundaries with HAZ1 and BM. These differences are attributed to the different thermal histories associated with the two substrate geometries and AFSD process parameters. The hardness data are again summarized in Table 5.

The sharp appearance of the interface between the substrate and cladding shown in Fig. 12, and the absence of a significant TMAZ below the deposited material, are similar to the characteristics observed in the groove-filling geometry, Figs. 4 and 6. Closer inspection of the interface reveals comparable localized mixing (Figs. 14a and 14b) and evidence of sensitization of the associated grain boundaries (Figs. 14c and 14d). Additional etching is visible in the interface between consecutive passes and along apparent flow lines (Fig. 14b). As above, the etch-pattern suggests that the shear mixing that bonds the interface has a potentially deleterious effect on the localized corrosion resistance of the filler alloy, possibly due to the formation of carbides enabled by incorporation of C from the graphite lubricant. Again, it is worth noting the oxalic acid etch is a sensitive screening test that may detect conditions which are not necessarily detrimental from a performance perspective [39]. As such, additional investigation of the corrosion resistance of AFSD 316L repairs represents a significant opportunity for future work.

The subsurface hardness of the AFSD 316L cladding was shown in Table 5 and Fig. 13 to be ~249 HV0.2, which is consistent with the normal surface hardness of 96 HRB determined by Rockwell testing. In contrast, the measured subsurface hardness of the as-received substrate provided in Table 4 is 426 HV0.2, while the normal surface hardness determined by Rockwell testing is 41 HRC. The difference in hardness between the as-received AISI 4340 substrate and the surface of the AFSD 316L filler material may raise some concern about loss of wear resistance resulting from the resurfacing. This was evaluated by performing two types of wear testing at the locations indicated W1 – W4 in Fig. 2b: two-body wear by abrasive loop contact, and erosion by solid particle impingement [31,32]. The results are provided in Table 7, from which it can be seen that the volume loss in the AFSD 316L is less than 70% of that in the as-received 4340 substrate during the two-body abrasion, regardless of the difference in hardness. The results also show that the mass loss during the erosion test was comparable for the two materials, differing by less than 3%.

**Table 7:** Wear rates during abrasive loop contact or erosion by particle impingement. Test locations are defined in Fig. 1.

Material	Test Location*	ASTM Method	Number of Tests	Average Volume Loss, mm <sup>3</sup>	Average Mass Loss, mg
4340	W1	G174 <sup>†</sup>	4	1.582	N/A
316L AFSD	W2	G174 <sup>†</sup>	4	1.086	N/A
316L AFSD	W3	G174 <sup>†</sup>	4	1.069	N/A
4340	W1	G76 <sup>‡</sup>	3	N/A	9.4
316L AFSD	W4	G76 <sup>‡</sup>	3	N/A	9.2

\* From Fig. 2

<sup>†</sup> Abrasion Resistance by Abrasive Loop Contact

<sup>‡</sup> Erosion by Solid Particle Impingement Using Gas Jets

Studies have shown a linear relation between hardness and abrasion resistance for steels with similar metallurgical phase compositions; however, recent work has also shown a strong dependence between wear resistance and phase composition during two-body abrasion of steels with the same initial hardness [41, 42]. Narayanaswamy, et al., investigated four steels with different microstructures, but all with hardness in the range of 325-360 HV, and reported wear rates in the following order: pearlite < bainite < martensite < tempered martensite [41]. In that work, for an abrasive (SiC) particle size of 58 microns, the relative two-body wear rates of the four phases were found to be 1.00, 1.36, 2.59 and 2.62, respectively. The differences in wear rate were attributed, in part, to the capacity of the two-phase microstructures (pearlite and bainite) to accommodate realignment of the harder carbide phase to the abrasion sliding direction by ductile deformation of the softer component. In addition, the lack of plastic deformation in the martensite and tempered martensite makes those phases more vulnerable to Hertzian fracture on the abrading surface, potentially leading to higher wear rates [43].

It is well established that austenitic stainless steels undergo strain-induced martensitic transformation in a near-surface layer during abrasive wear [44, 45, 46]. This creates a multi-phase microstructure that allows realignment of the harder martensite towards the abrasive sliding direction, and favors ploughing and wedge formation with narrow/deep surface tracks. In contrast, the tempered martensite of the AISI 4340 resists plastic deformation, thus favoring cutting (material loss) with wide/shallow surface tracks. Fig. 15 shows SEM images of the wear surface from the as-received AISI 4340 and the AFSD 316L, locations W1 and W2 in Fig. 2b. The images show deeper grooves with more plastic deformation and obvious

ploughing in the AFSD material, Fig. 15b. In contrast, the surface of the AISI 4340 in Fig. 15a exhibits shallower grooves with less evidence of plastic deformation, which is consistent with cutting as the dominant abrasion mechanism. In this context, it is noteworthy that the mechanisms involving plastic deformation during abrasive wear, ploughing and wedge formation, only deform/translate material, whereas cutting results in material removal. The current results for the two-body abrasive loop test, Table 7, are thus consistent with prior reports of elevated wear resistance in steel microstructures comprised of two-phases, hard and soft (brittle and ductile), relative to microstructures comprised of a single hard phase.

Material loss during erosion by particle impingement is generally thought to occur when the indent formed by an impinging particle creates a protruding rim of plastically deformed material that is later removed as wear debris [47]. In this case the formation of the rim is dependent upon the flow stress and ductility of the target material, and the removal of the rim as debris depends upon the work-hardening of the displaced material. Thus, it is thought that the elongation to failure plays a significant role in the resistance to erosion. In addition, sub-surface investigations on polished 316L have revealed the formation of a nanograined surface layer approximately 1 mm in depth, and have suggested that damage accumulation from particle impacts results in the formation of a strain-induced martensitic phase transformation [47]. As a result, the comparable performance of the as-received AISI 4340 and the AFSD 316L in the solid particle impingement test is not surprising.

Three-point bend testing was performed on the multi-layer cladding designated S1 in Fig. 2a, and for comparison on bare 4340 substrate. Fig. 16a shows the test configuration, where the span  $L$  is approximately 90 mm and the deflection  $D$  is such that the AFSD 316L is on the tensile side of the sample. Fig. 16b shows plots of the flexural stress  $\sigma_f$  versus flexural strain  $\epsilon_f$  for the bare and clad substrates, where

$$\sigma_f = \frac{3FL}{2bd^2}$$

4

$$\epsilon_f = \frac{6Dd}{L^2}$$

5

In Eqs. (4) and (5),  $F$ ,  $b$ , and  $d$  represent the applied load, sample width, and sample thickness, respectively. The results, which are summarized in Table 8, show that the yield and ultimate strengths of the clad sample are 60% and 73% of the unclad substrate, respectively. This is due to the lower tensile strength of the AFSD 316L relative to the 4340 substrate. The clad bar also shows improvement in the strain to failure of 47%, which is again attributable to the performance of the 316L cladding on the tensile side of the bar. Note from Table 8 that the samples were configured to be similar in thickness, 11.3 vs. 14.1 mm, but with approximately one half (52%) of the clad sample comprising cladding. Thus, the

interface between the cladding and substrate is approximately at the neutral axis, neglecting the slight difference in moduli, with the cladding in tension and the substrate in compression. Fig. 16c shows the clad sample after the bend test. Near the bottom of the image, it can be seen that the final AFSD layer has fractured and delaminated. This indicates poor interlayer bonding at this thickness of cladding (7.4 mm).

**Table 8:** Results of three-point bend testing.

	<b>4340 Substrate</b>	<b>316 AFSD / 4340</b>	<b>Change, %</b>
Yield Strength, MPa	2025	1224	-39.6
Ultimate Strength, MPa	2621	1912	-27.1
Strain at failure, %	7.6	11.2	47.4
Thickness 4340, mm	11.3	6.7	N/A
Thickness 316, mm	0	7.4	N/A
Total Thickness, mm	11.3	14.1	N/A

## 4.0 Summary And Conclusions

Possible repair strategies for AISI 4340 steel using AISI 316L deposited by AFSD were evaluated by metallography, microhardness, and wear and mechanical testing. Two repair geometries were investigated: groove-filling and surface cladding. The former represents repair of localized grinding to eliminate cracks, while the latter represents material replacement over a larger area, for example to repair general corrosion or wear. Compared to the as-received 316L, the microstructure in the AFSD 316L was significantly refined, with decreased grain size and no residual evidence of plastic deformation. Microhardness testing indicated a slight decrease in the hardness after AFSD, 3% - 12%, while tensile testing indicated a comparable strength decrease of 10% - 12%. Wear testing by two-body abrasion and erosion by particle impingement both indicated that the wear resistance of the AFSD 316L was as good as, or better than, the substrate 4340. Some evidence was observed to suggest that the resistance to intergranular corrosion was compromised in the AFSD 316L, whether due to diffusion of C from the graphite lubricant or to formation of sigma phase.

In both repair geometries, the microstructure of the substrate beneath the deposited material exhibited upper and lower heat affected zones, HAZ1 and HAZ2, respectively. The appearance and microhardness profiles of these zones suggests that in both HAZ's the substrate reached a sufficiently high temperature to transform to austenite. In HAZ1, the subsequent cooling rate was sufficiently rapid to transform the austenite to martensite, while in HAZ2 a slower cooling rate resulted in transformation to upper bainite. Below HAZ2, the temperature was never high enough to transform the material to austenite, and the substrate retained the original tempered martensite microstructure. An observed gradient in the grain size

in HAZ2, as well as the refined grain size relative to the original microstructure, suggest that the maximum (transformation) temperature in the HAZ's decreased with depth during the AFSD process. Future work should evaluate the impact of the martensite in HAZ1 upon the fracture toughness of the repaired material.

## Declarations

### *Funding*

This material is based upon work supported by the Office of Naval Research under Award No. N00014-18-1-2339.

### *Conflicts of interest/Competing interests*

The authors have no conflicts of interest to declare that are relevant to the content of this article.

### *Availability of data and material*

Data not available / The authors do not have permission to share data.

### *Code availability*

Not Applicable.

### *Ethics approval*

Not Applicable.

### *Consent to participate*

Not Applicable.

### *Consent for publication*

Not Applicable.

### *Authors' contributions*

The authors confirm contribution to the paper as follows: study conception and design: AL and MW; data collection: LPM and AL; analysis and interpretation of results: LPM and AL; Author draft manuscript: LPM. All authors reviewed the results and approved the final version of the manuscript.

## References

1. Hartley WD, Garcia D, Yoder JK, Poczatek E, Forsmark JH, Luckey SG, Dillard DA, Hang ZY (2021) Solid-state cladding on thin automotive sheet metals Enabled by additive friction stir deposition.

- Journal of Materials Processing Technology. 291:117045.  
<https://doi.org/10.1016/j.jmatprotec.2021.117045>
2. Hang ZY, Jones ME, Brady GW, Griffiths RJ, Garcia D, Rauch HA, Cox CD, Hardwick N (2018) Non-beam-based metal additive manufacturing enabled by additive friction stir deposition. *Scripta Materialia* 153:122-30. <https://doi.org/10.1016/j.scriptamat.2018.03.025>.
  3. Avery DZ, Rivera OG, Mason CJ, Phillips BJ, Jordon JB, Su J, Hardwick N, Allison PG (2018) Fatigue behavior of solid-state additive manufactured inconel 625. *JOM* 70(11):2475-84.
  4. Griffiths RJ, Perry ME, Sietins JM, Zhu Y, Hardwick N, Cox CD, Rauch HA, Hang ZY (2019) A perspective on solid-state additive manufacturing of aluminum matrix composites using MELD. *Journal of Materials Engineering and Performance* 28(2):648-56.
  5. Chen YC, Fujii H, Tsumura T, Kitagawa Y, Nakata K, Ikeuchi K, Matsubayashi K, Michishita Y, Fujiya Y, Katoh J (2009) Friction stir processing of 316L stainless steel plate. *Science and Technology of Welding and Joining* 14(3):197-201.
  6. Kandasamy K, Renaghan LE, Calvert JR, Creehan KD, Schultz JP (2013) Solid-state additive manufacturing of aluminum and magnesium alloys. *Proceedings of materials science and technology, Montreal, Quebec, Canada*:59-69.
  7. Gray DT (2009) Modeling and Characterization of Friction Stir Fabricated Coatings on Al6061 and Al5083 Substrates. Dissertation, Virginia Polytechnic Institute and State University.
  8. Rivera OG, Allison PG, Jordon JB, Rodriguez OL, Brewer LN, McClelland Z, Whittington WR, Francis D, Su J, Martens RL, Hardwick N (2017) Microstructures and mechanical behavior of Inconel 625 fabricated by solid-state additive manufacturing. *Materials Science and Engineering: A* 694:1-9. <https://doi.org/10.1016/j.msea.2017.03.105>.
  9. Avery DZ, Rivera OG, Mason CJ, Phillips BJ, Jordon JB, Su J, Hardwick N, Allison PG (2018) Fatigue behavior of solid-state additive manufactured inconel 625. *JOM* 70(11):2475-84.
  10. Priedeman JL, Phillips BJ, Lopez JJ, Tucker Roper BE, Hornbuckle BC, Darling KA, Jordon JB, Allison PG, Thompson GB (2020) Microstructure Development in Additive Friction Stir-Deposited Cu. *Metals* 10(11):1538.
  11. MELD Brochure – MELD Manufacturing Corporation. <http://meldmanufacturing.com/technology-overview/>
  12. Perry ME, Griffiths RJ, Garcia D, Sietins JM, Zhu Y, Hang ZY (2020) Morphological and microstructural investigation of the non-planar interface formed in solid-state metal additive manufacturing by additive friction stir deposition. *Additive Manufacturing* 35:101293.
  13. Griffiths RJ, Petersen DT, Garcia D, Yu HZ (2019) Additive friction stir-enabled solid-state additive manufacturing for the repair of 7075 aluminum alloy. *Applied Sciences* 9(17):3486.
  14. Rutherford BA, Avery DZ, Phillips BJ, Rao HM, Doherty KJ, Allison PG, Brewer LN, Jordon JB (2020) Effect of Thermomechanical Processing on Fatigue Behavior in Solid-State Additive Manufacturing of Al-Mg-Si Alloy. *Metals* 10(7):947.

15. Heidarzadeh A, Mironov S, Kaibyshev R, Çam G, Simar A, Gerlich A, Khodabakhshi F, Mostafaei A, Field DP, Robson JD, Deschamps A (2020) Friction stir welding/processing of metals and alloys: A comprehensive review on microstructural evolution. *Progress in Materials Science*:100752.
16. Çam G (2011) Friction stir welded structural materials: beyond Al-alloys. *International Materials Reviews* 56(1):1-48.
17. Liu FC, Hovanski Y, Miles MP, Sorensen CD, Nelson TW (2018) A review of friction stir welding of steels: Tool, material flow, microstructure, and properties. *Journal of Materials Science & Technology* 34(1):39-57.
18. Çam G, İpekoğlu G, Küçükömeroğlu T, and Aktarer SM (2017) Applicability of friction stir welding to steels. *Journal of Achievements in Materials and Manufacturing Engineering* 80(2): 65-85.
19. Küçükömeroğlu T, Aktarer SM, İpekoğlu G, and Çam G (2018) Microstructure and mechanical properties of friction-stir welded St52 steel joints. *International Journal of Minerals, Metallurgy, and Materials* 25(12):1457-1464.
20. Nandan R, DebRoy T, and Bhadeshia HKDH (2008) Recent advances in friction-stir welding–process, weldment structure and properties. *Progress in Materials Science* 53(6):980-1023.
21. Khodabakhshi F, and Gerlich AP (2018) Potentials and strategies of solid-state additive friction-stir manufacturing technology: A critical review, *Journal of Manufacturing Processes* 36:77-92.
22. Srivastava M, Rathee S, Maheshwari S, Noor Siddiquee A, Kundra TK (2019) A review on recent progress in solid state friction based metal additive manufacturing: friction stir additive techniques. *Critical Reviews in Solid State and Materials Sciences* 44(5):345-77.
23. Dilip JJS, Ram GDJ, and Stucker BE (2012) Additive manufacturing with friction welding and friction deposition processes. *International Journal of Rapid Manufacturing* 3(1):56-59.
24. Beladi H, Farabi E, Hodgson PD, Barnett MR, Rohrer GS, and Fabijanic D (2021) Microstructure evolution of 316L stainless steel during solid-state additive friction stir deposition. *Philosophical Magazine*:1-16.
25. Asiatico P, (2021) The Applicability of Additive friction Stir Deposition for Bridge Repair, Virginia Polytechnic Institute and State University.
26. Martin LP, Luccitti A, and Walluk M (2021) Repair of aluminum 6061 plate by additive friction stir deposition. *The International Journal of Advanced Manufacturing Technology*.  
<https://doi.org/10.1007/s00170-021-07953-z>.
27. Martin LP, Luccitti A, and Walluk M (2022) Evaluation of Additive Friction Stir Deposition for the Repair of Cast Al-1.4 Si-1.1 Cu-1.5 Mg-2.1 Zn. *Journal of Manufacturing Science and Engineering* 144(6). <https://doi.org/10.1115/1.4052759>.
28. Gottwald RB, Griffiths RJ, Petersen DT, Perry MEJ, and Yu HZ (2021) Solid-State Metal Additive Manufacturing for Structural Repair. *Accounts of Materials Research* 2(9):780-792.
29. Avery DZ, Cleek C, Phillips BJ, Rekha YR, Kinser RP, Rao H, Brewer L, Allison P, and Jordon JB (2021) Evaluation of Microstructure and Mechanical Properties of Al-Zn-Mg-Cu Alloy Repaired via Additive Friction Stir-Deposition. *Journal of Engineering Materials and Technology*: 1-35.

30. ASTM B557-15 (2015) Standard Test Methods for Tension Testing Wrought and Cast Aluminum- and Magnesium-Alloy Products, ASTM International, West Conshohocken, PA.
31. ASTM G174-04 (2017) Standard Test Method for Measuring Abrasion Resistance of Materials by Abrasive Loop Contact, ASTM International, West Conshohocken, PA.
32. ASTM G76-18 (2018) Standard Test Method for Conducting Erosion Tests by Solid Particle Impingement Using Gas Jets, ASTM International, West Conshohocken, PA.
33. Xu D, Xiangliang W, Jianxin Y, Guang X, and Guangqiang L (2018) Effect of cold deformation on microstructures and mechanical properties of austenitic stainless steel. *Metals* 8(7): 522.
34. ASTM E140-02 (2002) Standard Hardness Conversion Tables for Metals Relationship Among Brinell Hardness, Vickers Hardness, Rockwell Hardness, Superficial Hardness, Knoop Hardness, and Scleroscope Hardness, ASTM International, West Conshohocken, PA.
35. ASM International Handbook Committee (1996) ASM Specialty Handbook: Carbon and Alloy Steels, ASM International: 640.
36. ASTM A666-15 (2015) Standard Specification for Annealed or Cold-Worked Austenitic Stainless Steel Sheet, Strip, Plate, and Flat Bar, ASTM International, West Conshohocken, PA.
37. Sun S, Liu Q, and Brandt M (2012) Microstructure and mechanical properties of laser cladding repair of AISI 4340 steel. *Sciences* 1:9.
38. Grange RA, Hribal CR, and Porter LF (1977) Hardness of tempered martensite in carbon and low-alloy steels. *Metallurgical Transactions A* 8:1775-1785.
39. ASTM A262-15 (2015) Standard Practices for Detecting Susceptibility to Intergranular Attack in Austenitic Stainless Steels, ASTM International, West Conshohocken, PA.
40. Chen YC, Fujii H, Tsumura T, Kitagawa Y, Nakata K, Ikeuchi K, Matsubayashi K, Michishita Y, Fujiya Y, and Katoh J (2009) Friction stir processing of 316L stainless steel plate. *Science and Technology of Welding and Joining* 14:197-201.
41. Narayanaswamy B, Hodgson P, and Beladi H (2016) Comparisons of the two-body abrasive wear behaviour of four different ferrous microstructures with similar hardness levels. *Wear* 350: 155-165.
42. Bourithis L, Papadimitriou GD, and Sideris J (2006) Comparison of wear properties of tool steels AISI D2 and O1 with the same hardness. *Tribology International* 39(6):479-489.
43. Chattopadhyay R (2001) Surface wear: analysis, treatment, and prevention, ASM international, Materials Park, OH.
44. Lee Y-S, Kondo Y, and Okayasu M (2020) Friction-Induced Martensitic Transformation and Wear Properties of Stainless Steel under Dry and Wet Conditions. *Metals* 10(6):743.
45. Farias MCM, Souza RM, Sinatora A, and Tanaka DK (2007) The influence of applied load, sliding velocity and martensitic transformation on the unlubricated sliding wear of austenitic stainless steels. *Wear* 263(1-6): 773-781.
46. Liu E, Zhang Y, Zhu L, Zeng Z, and Gao R (2017) Effect of strain-induced martensite on the tribocorrosion of AISI 316L austenitic stainless steel in seawater. *Rsc Advances* 7(71):44923-44932.

47. Wood RJK, Walker JC, Harvey TJ, Wang S, and Rajahram SS (2013) Influence of microstructure on the erosion and erosion–corrosion characteristics of 316 stainless steel. *Wear* 306(1-2):254-262.

## Figures

Figure 1

Schematic illustrations of AFSD: a) plan view of surface cladding, showing the rotation and translation of the tool, and b) cross-sectional view along the translation direction during of groove-filling.

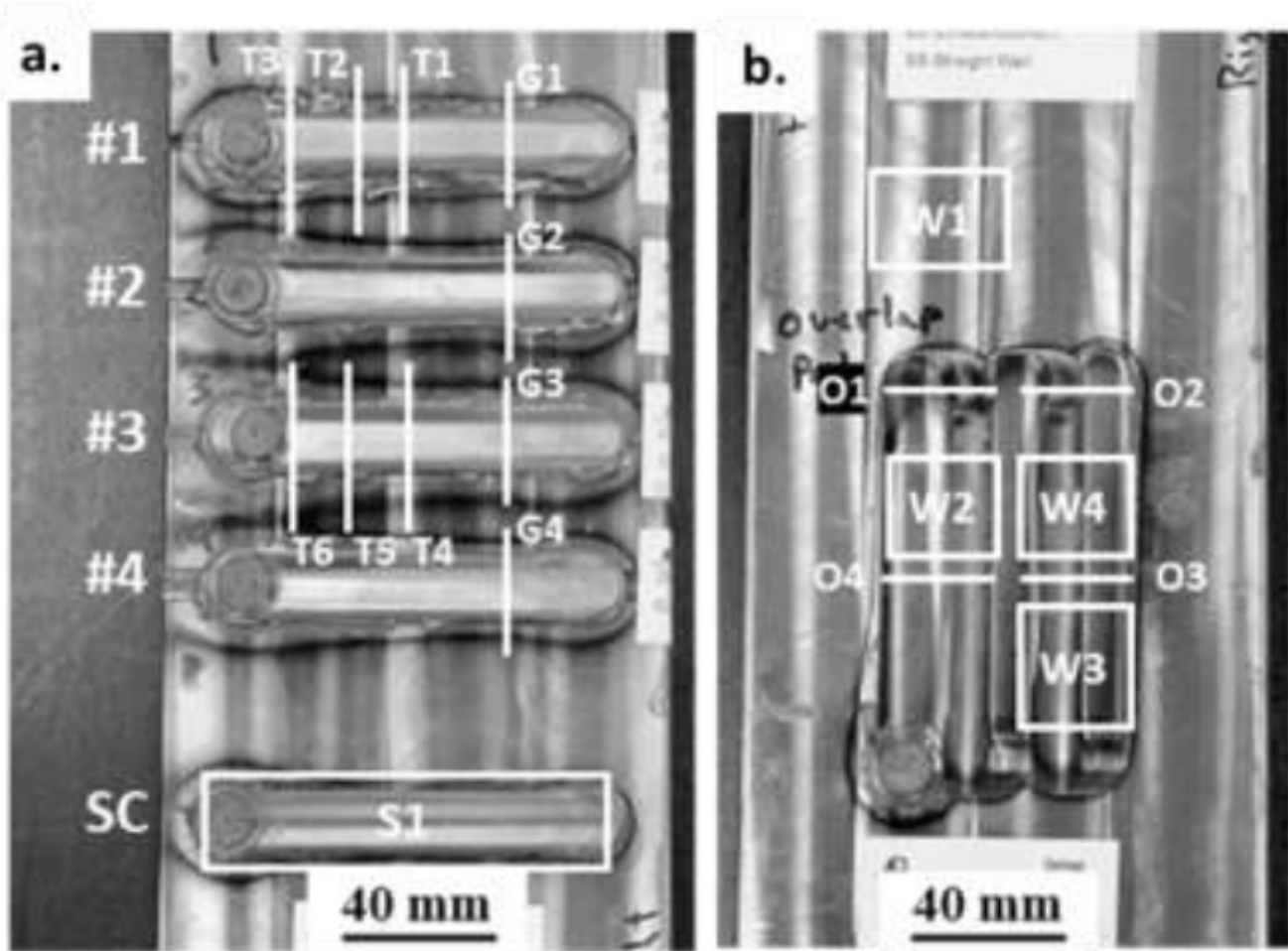


Figure 2

Macro-photograph of the plate with the AFSD deposition of AISI 316L to AISI 4340 plate: a) shows four short-groove repairs and one single-clad overlay, b) shows the overlap clad overlay.



### Figure 3

Microstructures of the as-received materials: (a,b) 316L filler alloy after etching with Kalling's reagent, and (c,d) 4340 substrate after etching with Vilella's reagent.

### Figure 4

Cross-sections from the metallurgical samples taken from the groove-filling locations defined in Table I: a) G1, b) G2, c) G3, and d) G4. The images show the AFSD 316L fill and overlay on the etched 4340 substrate. The numbers in (a) indicate the locations of the microstructures shown in Fig. 6: 1 - AFSD 316, 2 - HAZ1, 3 - HAZ2, and 4 - BM. The scalebar in (a) is valid for all four images.

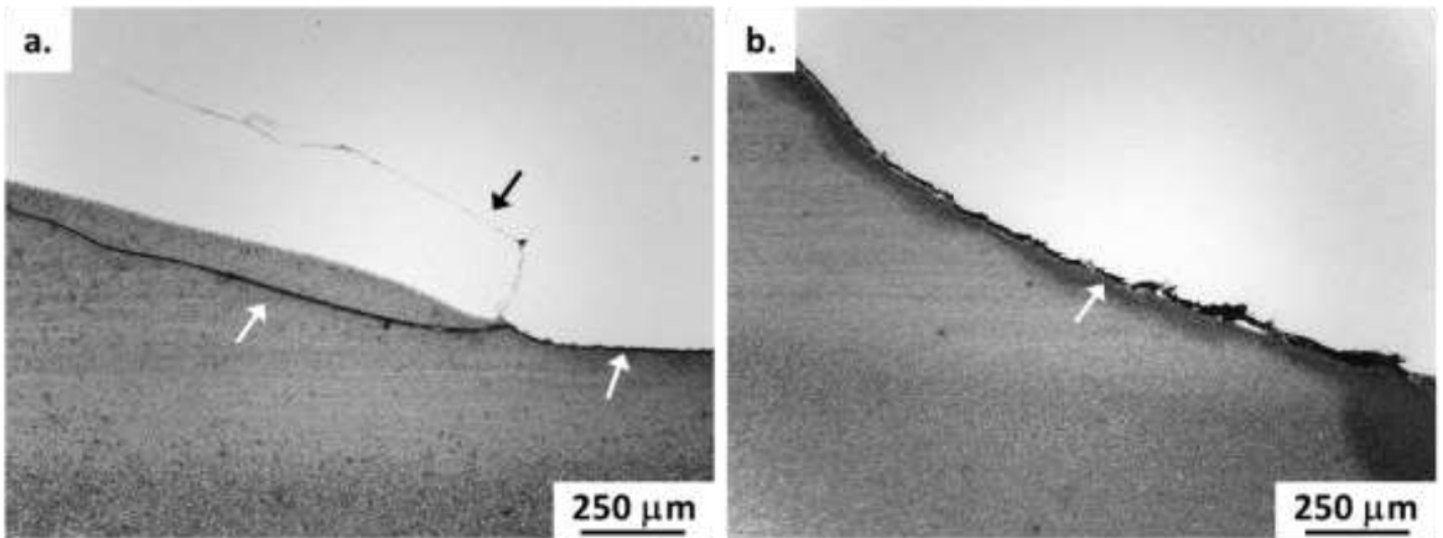


**Figure 5**

Showing cracks at the AFSD-substrate interface (white arrows) in the two deeper grooves: a) groove 2, section G2, and b) groove 4, section G4. The dark feature indicated by the black arrow in (a) is a line of inclusions.

**Figure 6**

Microstructures from the locations indicated in Fig. 4a for groove 1, section G1: a) AFSD 316L at location 1, b) martensite HAZ1 at location 2, c) upper bainite HAZ2 at location 3, and d) tempered martensite BM at location 4.

**Figure 7**

Scanning electron microscope (SEM) images of the microstructure from: a) bottom of HAZ2, and b) top of BM.

**Figure 8**

Depth profiles of the Vickers microhardness at the locations indicated by the dashed lines in Fig. 4: a) groove 1, section G1, and b) groove 2, section G2.



### Figure 9

LOM images showing localized mixing at the interface: a) the left edge of groove 1 in section G1, and b) the right edge of groove 3 in section G3.

### Figure 10

The microstructure from groove 1, section G1, after oxalic acid etching at  $1 \text{ A/cm}^2$  for 90 seconds to detect sensitization. The areas of (b) through (d) are indicated in images (a) through (c). Note that the field of view in (b) is approximately the same as Fig. 9a.

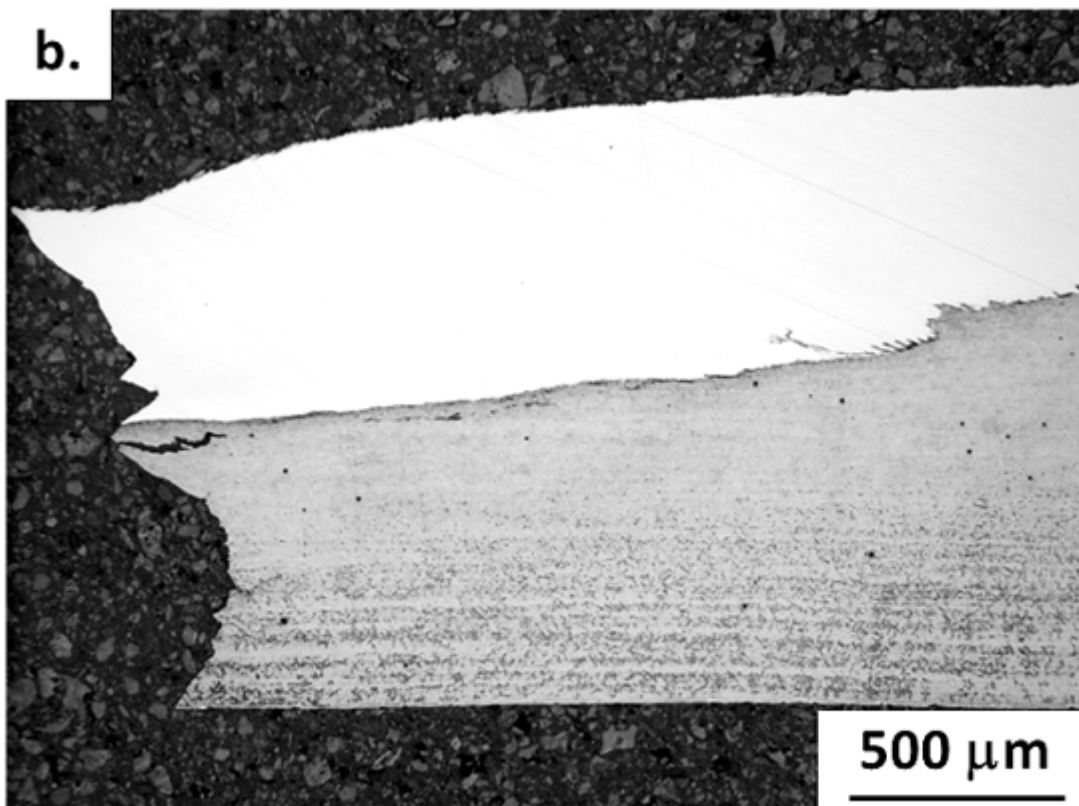


Figure 11

LOM images from cross-sections of the tensile failures from: a) sample T1 from groove 1, and b) sample T5 from groove 3.

Figure 12

Cross-sections from the metallurgical samples taken from the overlap cladding locations defined in Fig. 1: a) O1, b) O2, c) O3, and d) O4. The scalebar in (d) is valid for all four images. The dashed box in (c) indicates the field of view for Fig. 14a.

### **Figure 13**

Vickers microhardness depth profiles in the overlap cladding, taken at the locations indicated by the dashed lines in Fig. 12: a) section O3, and b) section O4.

### **Figure 14**

LOM images of the interface from overlap clad section O3: a) at the location indicated by the dashed box in Fig. 12c, prior to electrolytic oxalic acid etch, b) the same location at higher magnification after oxalic acid etch, c) along the interface with HAZ1 after oxalic acid etch, and d) SEM image taken after oxalic acid etch at the location indicated by the black arrow in (b).

### **Figure 15**

SEM images of the wear surfaces from the abrasive loop contact test: a) AISI 4340, location W1, and b) AFSD 316L, location W2.

### **Figure 16**

a) The 3-point bend test setup, b) The stress-strain behavior during the test, and c) the AFSD sample after the bend test.